A Fast BP Algorithm With Wavenumber Spectrum Fusion for High-Resolution Spotlight SAR Imaging

Lei Zhang, *Member, IEEE*, Hao-lin Li, Zhi-jun Qiao, *Member, IEEE*, and Zhi-wei Xu

***Abstract*—This letter presents the accelerated fast backprojection (AFBP) algorithm for high-resolution spotlight synthetic aperture radar (SAR) imaging. In conventional fast backprojection (FBP) algorithms, image-domain interpolation is employed in the subaperture (SA) fusion. However, in AFBP, by using a unified polar coordinate (UPC) system, the interpolation-based fusion is substituted by fusing the SA spectra in the wavenumber (WN) spectrum domain. The WN-domain SA fusion is efficiently implemented by fast Fourier transform and circular shifting. In this letter, an accurate impulse response function and the WN spectrum expression of the backprojected image in the UPC are explicitly derived, and furthermore, the implementations of AFBP are investigated in detail. Compared with conventional FBP algorithms, the AFBP can precisely focus on high-resolution SAR data with dramatically improved efficiency. Both simulation and real-measured data experiments validate the superiorities of AFBP by comparing it with the fast factorization backprojection (FFBP) algorithm.**

***Index Terms*—Accelerated fast BP (AFBP), fast backprojection (FBP), fast factorized backprojection (FFBP).**

I. Introduction

THE time-domain backprojection (BP) algorithm has already been recognized as an ideal approach for high-resolution synthetic aperture radar (SAR) imaging [1]–[3]. Rooted in the basic principle of wideband beamforming with the 2-D coherent integral, the BP algorithm offers more advantages than traditional SAR image formations, such as the precise compensation of curve wave-front effect for any SAR configuration optimal accommodation of topography and aperture-dependent motion compensation [4]–[7]. However, the intensive computational burden of the original BP algorithm makes it unacceptable in many real-time imaging scenarios. Hence, great efforts have been devoted to enhancing the efficiency of the BP integral. Several novel fast BP (FBP) algorithms have been recently developed [8]–[10], for instance, the fast factorized backprojection (FFBP) algorithm [9] is one of them. The key idea of the FFBP algorithm is to split the long synthetic aperture into short subapertures (SAs), each of which generates a coarse angular resolution image in a local polar coordinate (LPC) system. The coarse images are then recursively fused by image-domain interpolation. In a pyramid computational architecture, the FFBP dramatically reduces the computational burden of the original BP algorithm, which is close to the theoretical efficiency of conventional frequency-domain algorithms. In the FFBP, however, the LPC system is adopted for an SA image, where the SA center is defined as the origin. Hence, coordinates of a certain target vary from one SA image to another. As a result, in the SA fusion of the FFBP, interpolation in both range and azimuth is necessary to fuse all SA images. The 2-D pixel-by-pixel interpolation brings two outstanding negative effects: 1) the main source of the computational burden of the FFBP lies in the 2-D interpolation; and 2) the interpolation also brings inevitable errors in each FFBP recursion, and those errors would be transferred and accumulated during the recursions, which lead to focal degradation of the final SAR image. In particular, with the decrease in the SA length, the focal degradation becomes serious, which instinctively yields a tradeoff between precision and efficiency in FFBP imaging. Although some optimal interpolation kernels [11] are able to improve the performance of the FFBP, the negative effects induced by the 2-D interpolation are still distinctive.

In this letter, the accelerated FBP (AFBP) is proposed for the high-resolution spotlight SAR imaging. Different from the recursive architecture of the FFBP, the AFBP only contains two stages: SA image formation using a unified polar coordinate (UPC) and SA fusion in the 2-D wavenumber (WN) domain. By the formation of all SA images in the UPC, the interpolation-based SA fusion in the FFBP is substituted by a 1-D spectrum fusion in the 2-D WN domain. Based on the rigid derivation of the impulse response function (IRF) in the BP image under the UPC, implementation of the AFBP is investigated in detail. The SA fusion of the AFBP is efficiently realized by fast Fourier transform (FFT) and circular shifting. As the 2-D interpolation within the FFBP SA fusion is avoided, the AFBP obtains significant improvements in both efficiency and precision. Experimental comparisons for the FFBP and the AFBP are presented by using real-measured SAR data set.

II. Derivation of the AFBP Algorithm

A. Introduction of the FFBP Algorithm

Here, we introduce the signal model and the basic principle of the BP integral. The spotlight SAR geometry in the polar coordinate system is shown in Fig. 1, where the SAR platform moves along a straight-line flight track with a constant velocity v, and a synthetic aperture of length L is generated. The straight

Manuscript received September 16, 2013; revised December 2, 2013 and December 10, 2013; accepted December 13, 2013. This work was supported in part by the Fundamental Research Funds for the Central Universities under Grant K5051302001 and in part by the National Natural Science Foundation of China under Grant 61301280, Grant 61328103, and Grant 61301187.

L. Zhang, H. Li, and Z. Xu are with the National Laboratory of Radar Signal Processing, Xidian University, Xi'an 710071, China (e-mail: leizhang@xidian.edu.cn; lihaolin322@163.com; zwxu1990@gmail.com).

Z. Qiao is with the Department of Mathematics, University of Texas—Pan American, Edinburg, TX 78539-2999 USA (e-mail: qiao@utpa.edu).

Color versions of one or more of the figures in this paper are available online at http://ieeexplore.ieee.org.

Digital Object Identifier 10.1109/LGRS.2013.2295326

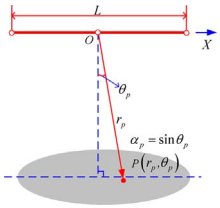

Fig. 1. Geometry of spotlight SAR in the polar coordinate geometry.

trajectory is defined as the X-axis with aperture centered at origin O. During data acquisition, the radar beam always illuminates the scene center. When the antenna phase center locates at $X = vt \in [-L/2, L/2)$ (where t denotes the slow time), the instantaneous range from the radar to a point target P in the polar coordinates (r_p, θ_p) is given by

$$R(X;r_p,\theta_p)=\sqrt{r_p^2+X^2-2r_pX\sin\theta_p},\quad -\frac{L}{2}\le X<\frac{L}{2}. \quad (1)$$

Defining the azimuth angular coordinate $\alpha_p = \sin\theta_p$, we can rewrite the range history as

$$R(X;r_p,\alpha_p)=\sqrt{r_p^2+X^2-2r_pX\alpha_p},\quad -\frac{L}{2}\le X<\frac{L}{2}. \quad (2)$$

Assuming that the point target has unit scattering coefficients, then after demodulation, we have the echoed signal of the target, i.e.,

$$s(\tau,X)=\text{rect}\left[\frac{X}{L}\right]\cdot s_T(\tau-\Delta t_p) \quad (3)$$

where $\Delta t_p = 2R(X;r_p,\alpha_p)/c$ corresponds to the time delay, c is the speed of light, and $s_T(\tau)$ is the transmitted waveform with bandwidth B and carrier frequency f_c. By the matched-filtering in range, the range-compressed signal is given by

$$s_M(\tau,X)=\text{sinc}\left[B\cdot(\tau-\Delta t_p)\right]\cdot\text{rect}\left[\frac{X}{L}\right]\cdot\exp\left[-jK_{rc}R(X;r_p,\alpha_p)\right] \quad (4)$$

where the sinc function is defined by $\text{sinc}(u) = \sin(\pi u)/\pi u$, symbol $K_{rc} = 4\pi/\lambda$ denotes the range WN center, and λ is the wavelength corresponding to the carrier frequency. The time-domain BP algorithm is implemented by a coherent integral along the range history in the range-compressed and azimuth time domain. The backprojected pixel at the coordinates (r_p, α_p) is obtained by a BP integral, i.e.,

$$S(r_p,\alpha_p)=\int_{-L/2}^{L/2}s_M\left[\tau=\frac{2R(X;r_p,\alpha_p)}{c},X\right]\cdot\exp\left[jK_{rc}R(X;r_p,\alpha_p)\right]dX. \quad (5)$$

For each pixel in the BP image, a coherent integral along a specific integral trajectory should be calculated in the 2-D range-compressed and azimuth time domain. In a pixel-by-pixel manner, BP imaging is inherently inefficient. Inheriting the precision merits of the BP algorithm, FBP algorithms [8], [9] are capable of accelerating the BP integral. One of such FBP algorithm is the FFBP, which divides the BP integral into SA BP integrals and combines the SA images coherently. In the first stage, the synthetic aperture is divided into a set of SAs, and each SA data is backprojected into an SA BP image with coarse angular resolution in an LPC system. The full-resolution SAR image is achieved by fusing all coarse images recursively,

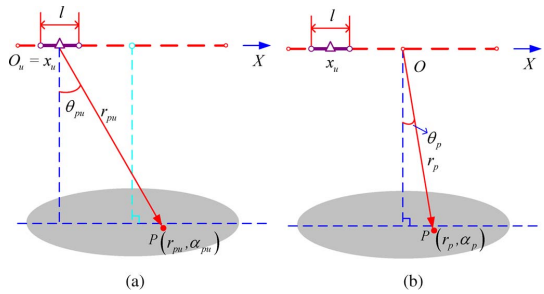

Fig. 2. Polar coordinates for SA imaging. (a) LPC. (b) UPC.

which usually contains several SA fusion stages. In each fusion stage, the LPC is established by setting the SA center as the coordinate origin. As shown in [8] and [9], BP imaging in the LPC is beneficial to avoid spectrum aliasing and ambiguity.

In the SA fusion of the original FFBP, a 2-D interpolation is required to combine all SA images in different LPCs together. For clarity, we use Fig. 2(a) to illuminate the LPC system in the SA imaging of the FFBP. In the following, we develop the AFBP algorithm. Without using the 2-D interpolation, the SA fusion of the AFBP relies on the spectrum connection implemented by the FFT and circular shifting. The key of the AFBP is that a UPC is utilized in the generation of SA images. Herein, we first interpret the concept of the UPC and compare it with the LPC. Let us split the full aperture into N_{sub} SAs with equal length $l = L/N_{sub}$. An SA image is generated with the BP integral in the first stage. However, all SAs are backprojected onto the UPC defined by (r, α). The coarse angular resolution SA image can be formed by the BP integral over the nth SA, i.e.,

$$I'_u(r,\alpha)=\int_{-l/2}^{l/2}s_M\left[\tau=\frac{2R(X+x_u;r,\alpha)}{c},X+x_u\right]\cdot\exp\left[jK_{rc}R(X+x_u;r,\alpha)\right]dX \quad (6)$$

where $x_u = (u - (N_{sub}/2) - (1/2)) \cdot l$ denotes the uth SA center. For our convenience, the UPC is set as the full-aperture polar coordinate shown in Fig. 2(b). Thus, all SA images are backprojected through using the UPC, namely, all SA images are mapped under the same polar coordinate system with the origin at O.

B. Accelerated FBP Algorithm

Here, we focus on the mathematical derivation and implementation of the AFBP algorithm. In order to facilitate the mathematical description, the IRF and its corresponding 2-D WN spectrum of the BP image in the UPC will be derived first.

The IRF for the point located at (r_p, α_p) in the UPC can be obtained through calculating the neighborhood pixels around the grid in the SA BP image. The IRF of the uth SA BP image is given as follows:

$$I_u(r,\alpha)=\int_{-l/2}^{l/2}s_M\left(\tau=\frac{2R(X+x_u;r,\alpha)}{c},X+x_u\right)\cdot\exp\left[jK_{rc}R(X+x_u;r,\alpha)\right]dX. \quad (7)$$

The magnitude of the IRF on grid (r, α) is achieved as a coherent integral of the range-compressed signal along the

range history $R(X+x_u;r,\alpha)$, and by replacing $X+x_u$ with X, (7) is simplified as

$$I_u(r,\alpha)=\int_{-l/2+x_u}^{l/2+x_u}\exp\left[-jK_{rc}\Delta R(X;r,\alpha)\right]dX. \quad (8)$$

In (8), $\Delta R(X;r,\alpha)$ stands for the difference between $R(X;r_p,\alpha_p)$ and $R(X;r_p,\alpha)$. To derive the analytic expression of the azimuth IRF, $\Delta R(X;r,\alpha)$ is extended into the second-order Taylor series, i.e.,

$$\begin{aligned}\Delta R(X;r_p,\alpha)&=R(X;r_p,\alpha_p)-R(X;r_p,\alpha)\\&=\sqrt{r_p^2+X^2-2Xr_p\alpha_p}-\sqrt{r_p^2+X^2-2Xr_p\alpha}\\&=(\alpha-\alpha_p)\cdot X+\frac{(\alpha^2-\alpha_p^2)}{2r_p}\cdot X^2+\sigma(X^3)\\&\qquad X\in\left[-\frac{l}{2},\frac{l}{2}\right)+x_u\\&\approx(\alpha-\alpha_p)\cdot X \quad (9)\end{aligned}$$

where $\sigma(X^3)$ represents the high-order terms, which usually take a fraction of $\Delta R(X;r_p,\alpha)$. In general, the vast majority of energy of IRF is intensively concentrated within a very small region around $\alpha=\alpha_p$, whose size is associated with the angular resolution. For the synthetic aperture of length L, the angular resolution is given by $\Delta\alpha=\lambda/2L$ [12]. Given a certain aperture length, the magnitude of the quadratic term in (9) increases as $(\alpha-\alpha_p)$ deviates from zero. Assuming that α is in the neighborhood of α_p that $\alpha=\alpha_p+\delta\alpha$, we can determine the effect of the quadratic term on the IRF as follows:

$$-\frac{\left(\alpha_p^2-\alpha^2\right)}{2r_p}\cdot X^2=-\frac{\left[\alpha_p^2-(\alpha_p+\delta\alpha)^2\right]}{2r_p}\cdot X^2\approx\frac{\delta\alpha\cdot\alpha_p}{r_p}\cdot X^2. \quad (10)$$

The quadratic term causes a quadratic phase error (QPE) in the BP integral in (8) as

$$\text{QPE}=4\pi\frac{\delta\alpha\cdot\alpha_p}{\lambda r_p}\cdot X^2. \quad (11)$$

The magnitude of QPE is directly proportional to $\delta\alpha$. Once the magnitude of QPE is small enough, its effect on the BP integral can be neglected, such as when QPE is constrained within $\pi/8$ [12]. As the shape of IRF is mainly determined by its magnitude within the range $[\alpha_p-\delta\alpha,\alpha_p+\delta\alpha]$, equivalently, the QPE at the boundary determines the shape of IRF. Substituting $\delta\alpha=\Delta\alpha$ into (11) and constraining the value of QPE below $\pi/8$, we have $|4\pi(\alpha_p/2L\cdot r_p)\cdot(L/2)^2|\le(\pi/8)$, which leads to $\alpha_pL\le(r_p/4)$. It indicates that, for the BP IRF, the first-order approximation in (9) is precise enough if the value of α_pL is smaller than a fourth of r_p. This constraint is easy to be achieved in real SAR scenarios.

In light of the azimuth IRF analysis, one can see that a nominal quadratic term makes the SA BP integral in (8) be simplified as

$$\begin{aligned}I_u(\alpha)&=\int_{-l/2+x_u}^{l/2+x_u}\exp\left[-j\cdot K_{rc}\cdot\Delta R(X;r_p,\alpha)\right]dX\\&\approx\int_{-l/2+x_u}^{l/2+x_u}\exp\left[-j\cdot K_{rc}\cdot X\cdot(\alpha-\alpha_p)\right]dX. \quad (12)\end{aligned}$$

To see the AFBP clearly, we define the angular WN variables as follows:

$$\begin{cases}K_\alpha=K_{rc}\cdot X\\ \Delta K_{\alpha u}=K_{rc}\cdot l\\ K_{\alpha u}=K_{rc}\cdot x_u.\end{cases} \quad (13)$$

Apparently, the angular WN K_α, interval $\Delta K_{\alpha u}$, and center $K_{\alpha u}$ are specifically associated with the azimuth coordinates X, SA length l, and SA center x_u, respectively. These variables reveal that there is an inherent correspondence between the azimuth time domain and the angular WN domain in the BP framework. By (13), (12) becomes

$$\begin{aligned}I_u(\alpha)=&\int_{-\Delta K_{\alpha u}/2+K_{\alpha u}}^{\Delta K_{\alpha u}/2+K_{\alpha u}}\\&\exp\left[-j\cdot K_\alpha\cdot(\alpha-\alpha_p)\right]dK_\alpha\quad \alpha\in\left[-\frac{\Delta A}{2},\frac{\Delta A}{2}\right] \quad (14)\end{aligned}$$

where ΔA is the predefined angular range of the SA image, which also determines the azimuth size of the final image. Obviously, the Fourier transform relationship between K_α and α yields a sinc expression of the azimuth IRF. This relationship paves a way for us to establish the SA fusion in the AFBP by seamlessly compositing the SA WN spectra. The expression of the angular WN spectrum is accessible via applying an inverse Fourier transform to $I_u(\alpha)$, i.e.,

$$\begin{aligned}I_u(K_\alpha)&=\int_{-\Delta A_u/2+A_{cu}}^{\Delta A_u/2+A_{cu}}I_u(\alpha)\cdot\exp(jK_\alpha\alpha)d\alpha\\&=\text{rect}\left[\frac{K_\alpha-K_{\alpha u}}{\Delta K_a}\right]\cdot\exp(jK_\alpha\alpha_p)\\&\qquad K_\alpha\in\left[-\frac{\Delta K_\alpha}{2},\frac{\Delta K_\alpha}{2}\right)+K_{\alpha u} \quad (15)\end{aligned}$$

where A_{cu} denotes the predefined coordinate center of the uth SA image in the UPC. The expression of $I_u(K_\alpha)$ in (15) is easy to understand: The window function determines the position and the width of the angular WN spectrum, and the exponential term corresponds to the azimuth grid of the target in the UPC. Redefining $\Delta\alpha$ as the interval of the angular grid, we note that the *Nyquist* sampling criteria can be satisfied only if the grid of the SA image is restricted by $\Delta\alpha\le\lambda/2l$. A crucial phenomenon should be noted: If $-(\Delta K_\alpha/2)+K_{\alpha u}<-(\pi/\Delta\alpha)$ or $(\Delta K_\alpha/2)+K_{\alpha u}>(\pi/\Delta\alpha)$, the angular WN spectrum would be folding, which is no matter to the SA fusion in the AFBP. For the uth SA, one can circularly shift the center of its angular WN spectrum from zero to $K_{\alpha u}$. Furthermore, (15) also indicates that, in the SA fusion of AFBP, each SA contributes an individual WN spectrum patch, whose WN center and width correspond to the SA center and its length, respectively. Based on above analysis, we can perform the SA fusion in the AFBP with the spectrum connection: Each angular WN spectrum is circularly shifted in the azimuth direction to move the WN center from zero to the WN center $K_{\alpha u}$, and they are united as a long vector, as illuminated in Fig. 3. The full-resolution SAR image is directly achieved by transforming the complete WN back into the image domain with a Fourier transform.

In order to implement the AFBP for high-resolution SAR imagery, we need to extend the WN connection to the 2-D case.

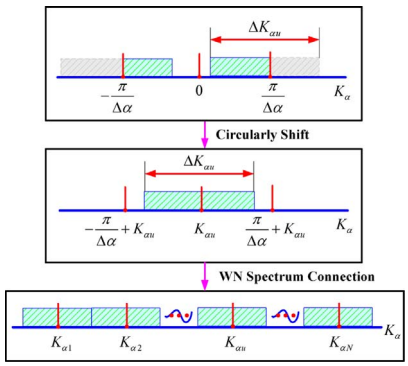

Fig. 3. SA fusion with angular WN spectrum connection.

The analytic 2-D WN spectrum can be directly extended from the 1-D spectrum expression in (12) through replacing the WN variables in (13) by

$$\begin{cases} K_\alpha = K_r \cdot X \\ \Delta K_{\alpha u} = K_r \cdot l \; K_r \in \left[-\frac{2\pi B}{c}, \frac{2\pi B}{c}\right] + K_{rc} \\ K_{\alpha u} = K_r \cdot x_u \end{cases} \tag{16}$$

where K_r is the range WN. By substituting (16) into (14) and (15), we arrive at the 2-D WN spectrum of the uth SA BP image, i.e.,

$$\begin{aligned} I_u(K_r, K_\alpha) =& \text{rect}\left[\frac{K_r - K_{rc}}{\Delta K_r}\right] \cdot \exp(-jK_r r_p) K_\alpha \\ &\in \left[-\frac{\Delta K_{\alpha u}}{2}, \frac{\Delta K_{\alpha u}}{2}\right) + K_{\alpha u} \\ &\cdot \text{rect}\left[\frac{K_\alpha - K_{\alpha u}}{\Delta K_a}\right] \cdot \exp(jK_\alpha \alpha_p) K_r \\ &\in \left[-\frac{\Delta K_r}{2}, \frac{\Delta K_r}{2}\right] + K_{rc} \end{aligned} \tag{17}$$

where $\Delta K_r = 4\pi B/c$ is the extent of range WN. From (16), we find that the WN center $K_{\alpha u}$ is a linear function of range WN K_r and that the 2-D WN spectrum is distributed in trapezoid form. With the variation of angular center with K_r, the angular WN spectrum connection in Fig. 3 can be extended immediately to the 2-D one, which implements the AFBP algorithm. Fig. 4 presents the spectrum connection processing of the AFBP. We may give a detailed procedure of the AFBP imaging in the following steps: 1) constructing SA images with coarse angular resolution in the UPC by using the BP integral; 2) applying the range FFT and azimuth inverse FFTs (IFFTs) to each SA image to transform them into the 2-D WN domain; 3) directly connecting the SA WN spectra to achieve the complete WN spectrum; and 4) the range IFFT and azimuth FFT are followed to obtain the full-resolution SAR image.

III. Real Data Experiments

Let us first evaluate the performance of the AFBP. A comparison with the original FFBP algorithm is also provided. The first stage of the FFBP is identical to that of the AFBP except in the selection of polar coordinates, while its SA fusion is implemented by 2-D interpolation recursively. For a fair comparison between the AFBP and the FFBP, the BP integral with an identical SA length is performed in the first stages of AFBP and FFBP. Full-resolution SAR images are obtained via

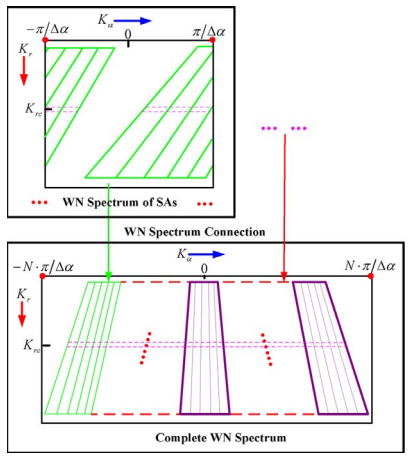

Fig. 4. SA fusion with 2-D WN spectrum connection.

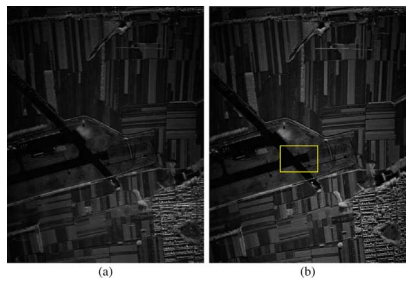

Fig. 5. (a) FFBP and (b) AFBP results.

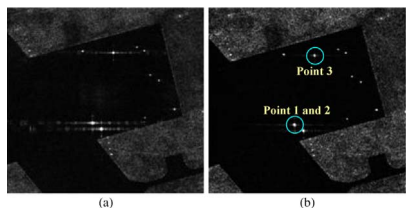

Fig. 6. Magnified subscene images of (a) FFBP and (b) AFBP.

spectrum connection in the AFBP and recursive interpolation-based fusion in the FFBP.

The tested data set was collected by an X-band experimental SAR working at a spotlight mode. Meanwhile, the pulse repetition frequency was 2100 Hz, and the transmitting signal bandwidth was 1.16 GHz. In our experiment, the synthetic aperture time was 7.8 s, acquiring 16 384 pulses with each pulse of 16 384 range bins. The closest operating range to the reference point was 10.5 km. The generated image was about 1.6 $\times$ 1.24 km in the range and azimuth directions with a nominal range and azimuth resolution of about 0.15 $\times$ 0.15 m. We produce high-resolution and wide-swath SAR imageries by both FFBP and AFBP, as presented in Fig. 5(a) and (b). Identical SA images are generated in the first stage of both FFBP and AFBP, where the synthetic aperture is evenly divided into 1024 SAs, each with length 16 pulses.

Using the spectrum connection for the SA fusion, the AFBP is over two times faster than the FFBP in this experiment. Both FFBP and AFBP achieve high-quality imageries. In fact, their difference is not distinguishable in vision from the

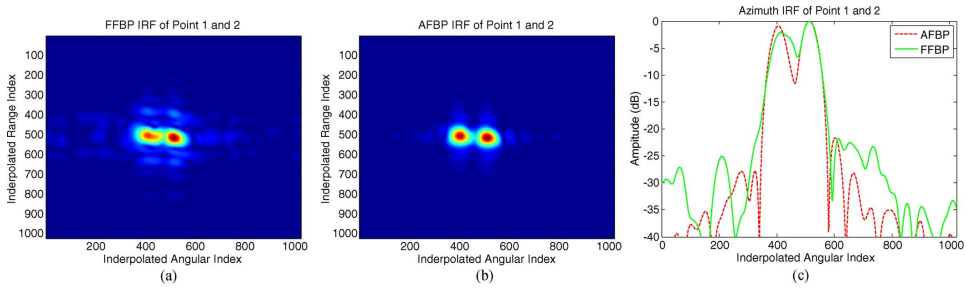

Fig. 7. Comparison of (a) FFBP and (b) AFBP images for points 1 and 2. (c) Azimuth IRF plots of points 1 and 2.

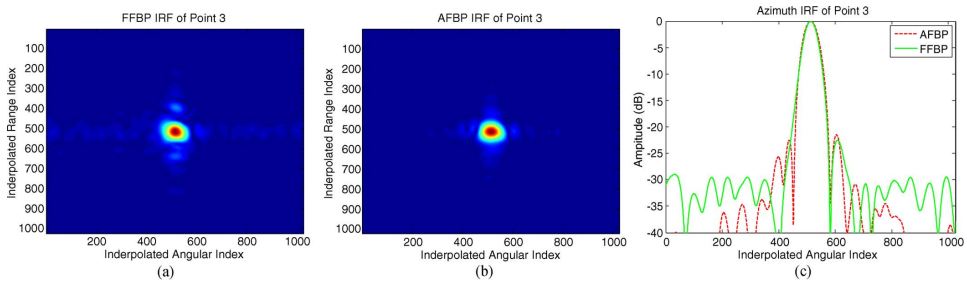

Fig. 8. Comparison of AFBP and FFBP images of point 3. (a) FFBP image of points 1 and 2. (b) AFBP image of point 3. (c) Azimuth IRF plots of point 3.

full-scene image. In order to access their performance comparison, a subscene in the imaging swath is magnified, as shown in Fig. 6, for a comparison. Particularly, the subscene contains some close-located trihedral corner reflectors, i.e., points 1–3 circled in Fig. 6(b). Although those point-like targets are optimally focused in both FFBP and AFBP images, those from the AFBP are focused with lower sidelobes, and their energy is more concentrated. The main reason for this phenomenon lies in that the interpolation error accumulation in the FFBP recursions is avoided in the AFBP. In subscene A, there are two close-located corner reflectors (points 1 and 2) with 0.15-m distance in azimuth and a single reflector (point 3), which are circled in the upper region in Fig. 6(b). To demonstrate the optimal performance of the proposed approach, we give their images and azimuth IRFs with hamming windowing in Figs. 7 and 8. One can clearly find that by both approaches, the two reflectors are distinctively separated, whereas the IRF distortion of the FFBP is obvious compared with the AFBP IRF. In Fig. 8(c), high sidelobes (up to -15 dB) exist near the main lobe, whereas the AFBP achieves much lower sidelobes (below -25 dB). We interpret that the high sidelobes in FFBP IRF can be reduced with the increase in SA length, *i.e.*, 64 pulses for an SA, at a price of significant increase in computational complexity. On the contrary, the AFBP can maintain its optimal performance with a short SA length, providing high efficiency simultaneously.

IV. Conclusion

This letter has proposed the AFBP algorithm for high-resolution spotlight SAR imaging. In the AFBP, SA images with coarse angular resolution are generated by mapping SA data into a UPC system. Based on the analytic expressions of the IRF, the SA fusion in conventional FFBP with interpolation is simplified into the processing of 1-D WN spectrum connection. Along with dramatic efficiency improvement, the AFBP can also reduce the undesired effects in the FFBP induced by the interpolation-based SA fusion.

Acknowledgment

The authors would like to thank the anonymous reviewers for their valuable comments that helped improve the letter quality.

References

[1] D. Munson, J. O'Brien, and W. Jenkins, "A tomographic formulation of spotlight-mode synthetic aperture radar," *Proc. IEEE*, vol. 71, no. 8, pp. 917–925, Aug. 1983.

[2] M. Desai and W. Jenkins, "Convolution backprojection image reconstruction for spotlight mode synthetic aperture radar," *IEEE Trans. Image Process.*, vol. 1, no. 4, pp. 505–517, Oct. 1992.

[3] C. Jakowatz, D. Wahl, and D. Yocky, "Beamforming as a foundation for spotlight-mode SAR image formation by backprojection," in *Proc. SPIE–Algorithms Synthetic Aperture Radar Imagery*, Mar. 2008, vol. 6970, p. 69700Q.

[4] O. Frey, C. Magnard, M. Rüegg, and E. Meier, "Focusing of airborne synthetic aperture radar data from highly nonlinear flight tracks," *IEEE Trans. Geosci. Remote Sens.*, vol. 47, no. 6, pp. 1844–1858, Jun. 2009.

[5] M. Rodriguez-cassola, P. Parts, G. Krieger, and A. Moreira, "Efficient time-domain image formation with precise topography accommodation for general bistatic SAR configurations," *IEEE Trans. Aerosp. Electron. Syst.*, vol. 47, no. 4, pp. 2949–2966, Oct. 2011.

[6] M. Soumekh, "Time domain non-linear SAR processing," Dept. Elect. Eng. State Univ. New York, New York, NY, USA, Tech. Rep., 2006.

[7] C. V. Jakowatz and D. E. Wahl, "Considerations for autofocus of spotlight-mode SAR imagery created using a beamforming algorithm," in *Proc. SPIE–Algorithms Synthetic Aperture Radar Imagery XVI*, 2009, vol. 7337, pp. 73370A-1–73370A-9.

[8] A. F. Yegulalp, "Fast backprojection algorithm for synthetic aperture radar," in *Proc. IEEE Radar Conf.*, Waltham, MA, USA, Apr. 20–22, 1999, pp. 60–65.

[9] L. M. H. Ulander, H. Hellsten, and G. Stenström, "Synthetic aperture radar processing using fast factorized back-projection," *IEEE Trans. Aerosp. Electron. Syst.*, vol. 39, no. 3, pp. 760–776, Jul. 2003.

[10] D. E. Wahl, D. A. Yocky, and C. V. Jakowatz, "An implementation of a fast backprojection image formation algorithm for spotlight-mode SAR," in *Proc. SPIE*, 2008, vol. 6970, pp. 69700H–69700H-11.

[11] P. O. Frölind and L. M. H. Ulander, "Evaluation of angular interpolation kernels in fast back-projection SAR processing," *IEE Proc. Radar Sonar Navigat.*, vol. 153, no. 3, pp. 243–249, Jun. 2006.

[12] W. G. Carrara, R. S. Goodman, and R. M. Majewski, *Spotlight Synthetic Aperture Radar: Signal Processing Algorithm [M]*. Boston, MA, USA: Artech House, 1995, pp. 245–254.